Structural relaxation of nanocrystalline PdAu alloy: Mapping pathways through the potential energy landscape

Michael Johannes Deckarm, Nils Boussard, Christian Braun, et al.

View Online Export Citation CrossMark

ARTICLES YOU MAY BE INTERESTED IN

Structural relaxation of nanocrystalline PdAu alloy: Probing the spectrum of potential barriers
Journal of Applied Physics **126**, 205102 (2019); https://doi.org/10.1063/1.5121520

Orientation mapping linked to fractal analysis: A method for studying abnormal grain growth in nanocrystalline PdAu
Journal of Applied Physics **128**, 185109 (2020); https://doi.org/10.1063/5.0029832

Some thermophysical properties of $(In_2Te_3)_{1-x}(Cd_{0.9}Zn_{0.1}Te)_x$ solid solutions
Journal of Applied Physics **127**, 125114 (2020); https://doi.org/10.1063/1.5140478

APL Quantum
CALL FOR APPLICANTS
Seeking Editor-in-Chief

Structural relaxation of nanocrystalline PdAu alloy: Mapping pathways through the potential energy landscape

View Online   Export Citation   CrossMark

Michael Johannes Deckarm,[a] [iD] Nils Boussard, Christian Braun,[a] [iD] and Rainer Birringer[a]

AFFILIATIONS

Department of Experimental Physics, Saarland University, Campus D2.2, 66123 Saarbrücken, Germany

[a]Authors to whom correspondence should be addressed: michael.deckarm@nano.uni-saarland.de;
c.braun@nano.uni-saarland.de; and r.birringer@nano.uni-saarland.de

ABSTRACT

Preparation history and processing have a crucial influence on which configurational state material systems assume. Glasses and nanocrystalline materials usually reside in nonequilibrium states at room temperature, and as a consequence, their thermodynamic, dynamical, and physical properties change with time—even years after manufacture. Such changes, entitled aging or structural relaxation, are all manifestations of paths taken in the underlying potential energy landscape. Since it is highly multidimensional, there is a need to reduce complexity. Here, we demonstrate how to construct a one-dimensional pathway across the energy landscape using strain/volume as an order parameter. On its way to equilibrium, we map the system's release of energy by calorimetry and the spectrum of barrier heights by dilatometry. The potential energy of the system is reduced by approximately $k_B T$ during relaxation, whereas the crossing of saddle points requires activation energies in the order of $1\,\mathrm{eV/atom}$ relative to the energy minima. As a consequence, the system behaves as a bad global minimum finder. We also discovered that aging is accompanied by a decrease in the non-ergodicity parameter, suggesting a decline in density fluctuations during aging.

I. INTRODUCTION

It is widely recognized that disordered solids, such as amorphous or nanostructured materials, are not in equilibrium relative to a laboratory time scale. As a consequence, their thermodynamic, dynamic, and physical properties change with time—even years after the time of manufacture. This change in properties with time far from equilibrium is termed aging or structural relaxation.[1,2] The latter term suggests that the underlying microscopic processes cause configurational rearrangements in the system, which result in changes in state variables (e.g., volume, enthalpy) as well as physical properties.[2] It is well established that both kinetic and thermodynamic properties of a system depend on its potential energy Φ,[3,4] which is a function of the configuration of the system. It is characterized by the positions of all N constituting particles (atoms, molecules, etc.), represented by N independent position vectors $\vec{r}_1, \ldots, \vec{r}_N$. These vectors span the $3N$-dimensional configuration space, in which each specific configuration (arrangement of particles) is represented

by a single point. Expanding this configuration space by the additional dimension of potential energy, the latter can be represented as a hypersurface in a $(3N + 1)$-dimensional space. The rugged character of such hypersurfaces inspired the potential energy landscape (PEL) paradigm to emphasize the relevance of the topographic features of these hypersurfaces, that is, inherent structures, basins, saddle points, and metabasins.[5,6]

The term inherent structure is assigned to local minima configurations of the PEL with respect to variations in the particle coordinates. A considerable reduction of the complexity of the PEL is achieved by partitioning the configuration space into nonoverlapping so-called basins of attraction, one for each inherent structure. Partitioning is obtained by the steepest descend mapping on the Φ hypersurface.[4] This means that an initial configuration of the N particles evolves along a steepest descend pathway or trajectory downward on the Φ hypersurface until all forces (gradients in Φ) vanish at a configuration of mechanical equilibrium. The corresponding unique

inherent structure j is represented by the point at the minimum on the Φ hypersurface and its basin encompasses the set of all configurations that converge on the inherent structure j.[6]

The shared boundaries between neighboring basins [$(3N-1)$-dimensional hypersurfaces] contain vanishing-gradient saddle points, which manifest transition states that separate the inherent structures. Structural relaxation kinetics typically involves thermally activated crossing of saddle points between neighboring basins. The energy difference between saddle points and the inherent structure defines the height of the energy barriers that separate these basins.[6]

The organization of adjacent basins into a larger valley is termed metabasin as schematically shown in Fig. 1. The energy barriers that have to be crossed to escape from the bottom of a metabasin are substantially larger compared to intra-metabasin barriers.[6]

The concept of potential energy landscape has been widely used to study relaxation, aging, and rejuvenation phenomena in supercooled liquids and glasses.[5,7–11] Aging/structural relaxation is a general phenomenon; therefore, it is not restricted to the glassy state but should be found in all kinds of disordered bulk materials irrespective of their chemical nature and of their atomic structure or microstructure.[12] From this perspective, we recently started to study structural relaxation in nanocrystalline $Pd_{90}Au_{10}$ by exploiting strain/volume release as an order parameter that accompanies the system's pathway/trajectory across the landscape. We found that the trajectory toward global equilibrium involved a spectrum of activation energies (barrier heights) to surmount the transition states.[13]

It is the goal of this study to also access—in addition to the activation energies—the energy of inherent structures traversed by the trajectory of the system on the PEL toward global energy minimum. Bringing together the information about transition states as well as local energy minima, curvature, and asymmetry of basins, it becomes feasible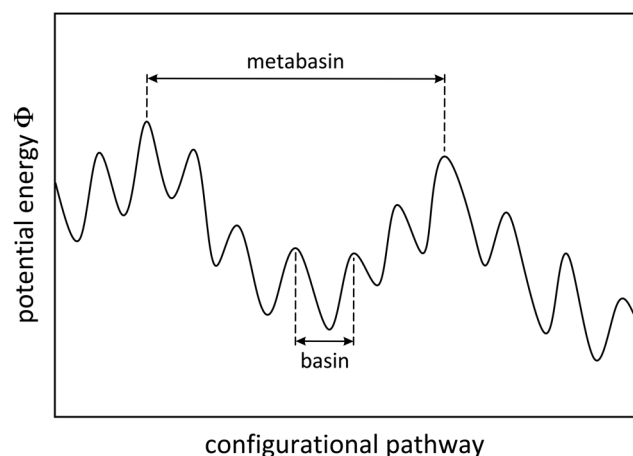 to map out relevant aspects of the topography of the PEL. In order to make the PEL concept applicable to laboratory experiments, it is required to introduce appropriate variants of the constant-volume and temperature-independent potential energy functions discussed so far. Moreover, the information extracted from experiments asks for adapting the PEL concept to a one-dimensional data basis.

II. MAPPING THE ENTHALPY FUNCTION

To define terminology and the scope of what remains to be done, we refer to Fig. 2. The displayed diagram,[13] inspired by the canonical glass-science diagram,[14] illustrates how extensive quantities of nanocrystalline (NC) materials,[15] such as enthalpy, entropy, and volume, are related to temperature. The crystalline ground state entails genuine reversible behavior in all regimes I, II, and III below the melting temperature T_m, thus providing a well defined reference state for measuring enthalpy differences.

Regime I represents a multitude of configurationally frozen and far out of equilibrium states of NC materials at different levels of enthalpy (volume, entropy, etc.). Below temperature T_{cf}, the materials behave essentially reversible. The amount of stored excess enthalpy—relative to the crystalline reference state—depends on the details of preparation and processing conditions. Two prominent synthesis
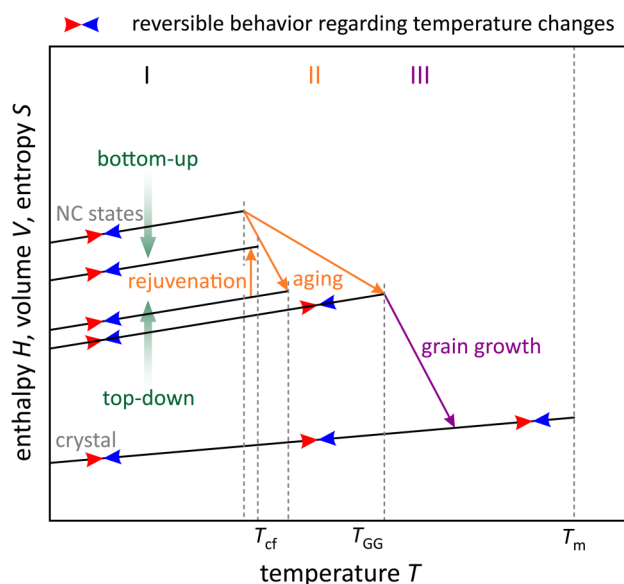

FIG. 2. Schematic of the evolution of state variables: enthalpy H, volume V, and entropy S of a nanocrystalline material as a function of temperature. Reproduced from Deckarm *et al.*, J. Appl. Phys. **126**, 205102 (2019), licensed under a Creative Commons Attribution (CC BY 4.0) license. The nanocrystalline states manifest elevated energies compared to the crystalline reference state. The green arrows indicate distinguished synthesis routes enabling to enter the nanocrystalline domain, either by energizing (top-down) or de-energizing (bottom-up) bulk or atomic/molecular material states; the arrowheads symbolize the direction, however, are not meant to mark specific enthalpy values of nanocrystalline states. For details about the different regimes (I–III), we refer to the text.

FIG. 1. Schematic plot of the potential energy Φ along a representative path through the configuration space to visualize the terms basin and metabasin.

strategies are indicated in Fig. 2: the bottom-up route, starting from individual atoms or molecules and forming nanoscale structures by condensation reactions,[16] and the top-down approach which is based on energizing and refining the microstructure of coarse-grained material states.[17]

Increasing the temperature above T_{cf} into regime II goes along with a reduction of free energy which involves enthalpy release through structural relaxation[18–20] and, in general, grain growth that is dominating enthalpy release in regime III.[21,22] In NC metals, a strict separation of these processes generally fails.[21] Nevertheless, we can identify time–temperature settings, which allow one to study structural relaxation dynamics at practically constant grain size. In this regime, located in between T_{cf} and T_{GG}, we have recently modeled the kinetics of volume relaxation in NC $Pd_{90}Au_{10}$ by partitioning the overall process into a set of independent and parallel reactions for arbitrary time–temperature protocols.[13] As a key result, we found that the intrinsic relaxation dynamics is heterogeneous—different from the commonly assumed stretched-exponential behavior[23,24]—and is characterized by a *spectrum* of Gibbs free energies of activation that are required to surmount the energy barriers the system encounters along its trajectory on the PEL.

In order to make the PEL concept applicable to laboratory experiments, it is necessary to introduce variants of the potential energy function Φ. We begin with the potential enthalpy Φ_H. While Φ refers to constant-volume scenarios, $\Phi_H = \Phi + PV$ classifies constant pressure P inherent structures and basins on its corresponding Φ_H hypersurface by isobaric steepest descent mapping.[6] In experiments, we couple the system to pressure and temperature reservoirs at fixed mole numbers of particles so that the connection to thermodynamics asks for the Gibbs free energy. We note that with increasing temperature, vibrational displacements away from the inherent-structure configurations become larger and eventually anharmonic contributions become significant. For isothermal-isobaric conditions, the Gibbs potential can be written as $G = \Phi_H + Nf_{vib}$, where f_{vib} represents a mean vibrational free energy per particle in the Φ_H ensemble, including all anharmonic effects. This particular expression for G is perfectly adapted to the PEL concept since it separates purely configurational aspects through Φ_H from purely vibrational aspects taken into account by f_{vib}.[6]

In laboratory experiments, such separation does not hold. It is the Gibbs free energy formulated in Callen's approach[25] $G(T, P, N, A_{GBa}) = H - TS + \gamma A_{GB}$, which enables to analyze the energetics of our NC material system; here S denotes the entropy, A_{GB} the overall interface/grain boundary (GB) area, and $\gamma = \partial G/\partial A_{GB}$, taken at fixed T, P, N, defines the intensive interface or GB free energy. In this approach, we assume that energy changes associated with structural changes are entirely represented by the (γA_{GB})-term. In contrast to the above Φ_H scenario, $H(S, P, N, A_{GBa})$ designates the enthalpy which also comprises vibrational contributions. Experimentally, we determine enthalpy *differences* ΔH between different material states. However, in Fig. 3, the potential enthalpy difference $\Delta \Phi_H$ between neighboring inherent structures is displayed, and the energy barrier height is denoted by ΔG^*. Although we consider only differences, $\Delta \Phi_H \neq \Delta H$ because computing differences in ΔH corresponds to material states which in general exhibit different specific heat c_p values. As a result, $\Delta H - \Delta \Phi_H \approx \int \Delta c_p(T) \, dT$. Or in other words, when we determine
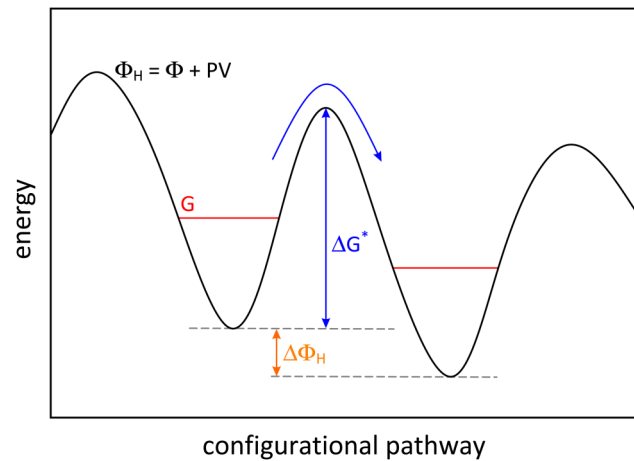

FIG. 3. Schematic plot of the potential enthalpy Φ_H (black line) along a path through the configuration space. The transition from the left to the right basin requires overcoming the barrier height ΔG^* and results in a potential enthalpy release $\Delta \Phi_H$. The Gibbs free energy in both basins is indicated in red.

ΔH by calorimetry through heat exchange $\Delta Q = \Delta H$, we extract a lower bound value for Φ_H since $\Delta c_p(T) < 0$.[26]

The experimentally prescribed isothermal-isobaric condition in conjunction with a fixed particle number implies that, in the one-dimensional energy representation in Fig. 3, the Gibbs free energy G must be a constant for any basin. However, its absolute value scales with the minima of PEL basins, and as a consequence, interbasin transitions may involve changes in G. Whenever $\Delta G < 0$, it acts as a driving force for each interbasin transition, the sequence of which represents the path on the PEL toward global energy minimum. We approximate $\Delta G \approx \Delta(\gamma A_{GB}) = A_{GB}\Delta\gamma + \gamma\Delta A_{GB}$. The first term on the RHS represents a decrease in γ at constant A_{GB} which complies with the notion of GB relaxation, where the core structure of GBs transforms from a nonequilibrium to equilibrated structure. The second term involves grain growth implying decreasing A_{GB} at basically fixed γ. We note that, in experiments, ΔH differences are measured; therefore, we have only access to the enthalpic part γ_H of the grain boundary free energy γ, which is, however, by far dominating γ since its entropic part $\gamma_S = -\partial\gamma/\partial T$ contributes with approximately 10^{-4} J/m^2 K.[27,28]

It seems appropriate to discuss the ($A_{GB}\Delta\gamma$)-term in some more detail. In NC metals, the crystal lattices of nanocrystals and their conjoined GBs are in mechanical equilibrium requiring that the absolute values of the components of the stress tensor σ_{ij} are continuous across the interfaces. Because of the reduction of the effective elastic moduli of GBs relative to the grain interior,[29,30] they are subjected to higher effective strains ε_{ij} and thereby capable of storing higher energy densities $w = \sigma_{ij}\varepsilon_{ij}$ than the grain interior. Moreover, molecular dynamics simulations reveal the presence of inhomogeneous strain concentration in the near vicinity of interfaces.[31,32] We may, therefore, assume that the enthalpy release in regime II is dominated by interfacial relaxation dynamics, which mainly involves the structural rearrangement in the core region of

GBs. However, mechanical coupling of interfacial relaxation to the abutting nanocrystals cannot be ruled out. Likewise, strain energy associated with the presence of defects (dislocations, stacking faults, twins, excess vacancies) in the interior of nanocrystals may also affect the relaxation dynamics.

For comparison with pertinent literature data, we, nevertheless, compute interfacial energy changes by attributing the measured enthalpy release upon GB relaxation to the corresponding total GB area. However, we like to point out that for construction and interpretation of the PEL, we have to refer to more general molar/volume averaged quantities since we have no information on the number and locations of relaxing atoms. Finally, we note that working with molar/volume averaged quantities offers the advantage to determine the curvature at the bottom of potential energy basins by measuring ultrasound propagation and extracting elastic constants. Regardless of whether the samples represent material states in the different regimes I–III, they behave statistically isotropically, and hence the determination of curvature reduces to measure bulk and shear modulus.

Regarding terminology,[2] we use the term annealing in its most general sense, that is, any time–temperature processing of specimens at elevated temperatures. This includes the commonly used isothermal and constant heating/cooling rate methods, as well as combinations thereof and nonlinear heating/cooling. During annealing, we measure the time evolution of enthalpy or volume (length) *release*. Processes that contribute to free energy *reduction* are commonly labeled *enthalpy recovery, (physical) aging* or *(structural) relaxation*. In this article, we will use the term structural relaxation and aging synonymously.

III. MATERIALS AND METHODS

A. Sample synthesis and preparation

The NC $Pd_{90}Au_{10}$ samples were synthesized by inert gas condensation[16] (IGC) using an ultrahigh-vacuum system (base pressure of 10^{-7} mbar) and thermal evaporation of high purity Pd and Au wires in a 6 mbar helium atmosphere. The nanocrystalline powder was subsequently transferred to a piston and anvil device and compacted under high vacuum ($<10^{-6}$ mbar) at a pressure of 1.8 GPa for a time period of 30 s to obtain disk-shaped samples (pellets) with a diameter of 8 mm, a thickness of 500–600 μm, and an initial grain size of ≈ 10 nm. For the studies presented in this paper, a single inert gas condensed pellet was synthesized and then cut—analog to Ref. 13—into four square pieces with an edge length of 2 mm and located around the pellet center; cutting was performed with a precision saw (*Buehler Isomet 1000*) equipped with a diamond blade.

IGC-prepared NC metals are distinguished by a random texture and a random interface orientation distribution function,[33] basically equiaxed grain shape and a lognormal grain size distribution function.[34] Hence, they can be considered prototypical random polycrystals, however, with enhanced localized stress and strain fluctuations due to the initial incompatibility of abutting crystallite shapes. Therefore, they seem predestined candidate materials to study nonequilibrium relaxation and related physical aging phenomena; the presence of pronounced anisotropies (texture) and/or macroscopic inhomogeneities would tremendously complicate the task.

B. Dilatometry

The macroscopic length change during thermal annealing was measured using a *Netzsch TMA402 Hyperion* dilatometer with a temperature range from $-150\,°C$ to $1000\,°C$. The specimens were positioned on a silica sample holder and contacted by a push rod with a circular contact area of 1 mm diameter by applying a force of 50 mN. Thermal expansion of the silica sample holder was corrected automatically via the built-in calibration function of the *Netzsch Proteus Analysis* software. Furthermore, the reversible thermal expansion of the NC material was estimated by linear thermal expansion with a mean expansion coefficient $\langle \alpha \rangle$ and subtracted from the measured length change in order to extract the irreversible length change only. In detail, the mean expansion coefficient $\langle \alpha \rangle$ was averaged over the initial linear expansion of the as-prepared (ap) samples close to room temperature (below $26\,°C$), which resulted in $\alpha_{ap} = 12.9(5) \times 10^{-6}\,K^{-1}$, and the linear cooling segment after relaxation, which yielded $\alpha_{rel} = 12.0(1) \times 10^{-6}\,K^{-1}$ in the relaxed (rel) state. As a result, we obtain $\langle \alpha \rangle = 12.5 \times 10^{-6}\,K^{-1}$. Since thermal expansion is a direct consequence of the asymmetry of the interatomic interaction potential, the decrease of α as a consequence of relaxation indicates a reduction of said asymmetry. Moreover, the thermal expansion coefficient after relaxation α_{rel} shows good agreement to the value for the conventional coarse-grained (cg) material of the same composition $\alpha_{cg} = 12.0(1) \times 10^{-6}\,K^{-1}$ reported in Ref. 35. After the correction of the reversible thermal expansion, the remaining irreversible length changes ΔL were related to initial length L_0 in the measuring direction to obtain the corresponding engineering strain $\varepsilon = \Delta L / L_0$.

C. Calorimetry

In addition to dilatometry, samples were analyzed with respect to stored specific enthalpy by calorimetry using a *DSC Q2000* differential scanning calorimeter from *TA Instruments* (temperature range from –90°C to 550°C). We performed two scans following each other immediately by using the same time–temperature protocol. The specific heat flux signal of the second measurement then served as a baseline and was subtracted from the first measurement to exclusively obtain the signature of irreversible processes. Enthalpy changes were calculated by integrating the specific heat flux difference over time. For error estimation, we analyzed the zero line drift in the respective annealing mode and temperature range to obtain an enthalpy error per integrated second which was multiplied by integration time. In parallel to dilatometry, the time–temperature protocols for the different experiments are introduced in Sec. IV.

D. Microstructural characterization

The grain size in the NC regime was determined by XRD measurements using a *Panalytical X'Pert Pro* diffractometer in θ–θ geometry equipped with a Cu-cathode and a PIXcel-1D detector. X-ray spectra covering a 2θ-range from $30°$ to $140°$ were recorded with $0.026°$ step size and 480 s measuring time per step. After fitting the peaks with Pearson VII functions in the *Panalytical HighScore* software, the volume-weighted average grain size $\langle D \rangle_{vol}$ was determined by the Klug and Alexander method as described in

Refs. 36 and 37. After grain growth, the grain size was analyzed by electron backscatter diffraction (EBSD) and orientation imaging microscopy (OIM) using a SEM *7000F* from *Jeol* in combination with an *EDAX/TSL digiview 3* camera.

The bulk density ρ_{bulk}, i.e., the density of the sample including closed porosity, was determined by the method of Archimedes.[38] Therefore, a microbalance *Sartorius R160P* with a resolution of 0.01 mg was used to measure the mass of the samples in the reference media air and diethyl phthalate (DEP). Each mass was determined ten times in both media and averaged for density calculation.

A further microstructural parameter in this work is the overall GB area A_{GB} of the specimen. For the GB area per unit volume of crystal, A_{GB}/V, stereology delivers the identity $A_{\text{GB}}/V = 2/\langle L \rangle_{\text{area}}$, where $\langle L \rangle_{\text{area}}$ denotes the area-weighted average column length of the grains. As derived by Krill and Birringer,[34] $\langle L \rangle_{\text{area}}$ can be computed when $\langle D \rangle_{\text{vol}}$ and the width σ of the lognormal size distribution are known, and hence, it results in

$$A_{\text{GB}} = \frac{m}{\rho_{\text{bulk}}} \cdot \frac{3}{\langle D \rangle_{\text{vol}}} \exp\left(\ln^2 \sigma\right), \quad (1)$$

where volume V was replaced by the quotient of sample mass m and bulk density ρ_{bulk}. For σ, we use a value of 1.7 that is a characteristic for IGC-prepared samples.[34]

E. Mechanical properties

To determine the elastic moduli, the samples were coupled to a 20 MHz ultrasonic transducer (*Panametrics V2173*), capable of simultaneously transmitting longitudinal and transversal waves. The pulse-echo patterns of the waves were monitored using a *LeCroy Wave Runner 6051* digital oscilloscope, and the time of flight can be computed applying the pulse-echo-overlap method.[39] The velocities for longitudinal and transversal waves, v_l and v_t, are given by $v = 2d/t$, where d is the specimen thickness, measured by a micrometer screw, and t is the respective time of flight. Assuming a quasi-isotropic material and linear elasticity, the shear modulus G and bulk modulus B can be determined according to the relations[29,40]

$$G = \rho_{\text{bulk}} \, v_t^2, \quad (2)$$

$$B = \frac{\rho_{\text{bulk}}}{3} \left(3v_l^2 - 4v_t^2\right), \quad (3)$$

with the sound velocities and the bulk density ρ_{bulk} as input parameters.

The plastic behavior was probed by Vickers hardness measurements performed on a *Frank Durotest 38151* testing device, where a force of 980 mN (HV 0.1) was applied for 30 s for each indent. The given hardness values represent the arithmetic mean of nine indents taken on the front and back sides of the sample, respectively.

IV. RESULTS AND DISCUSSION

To investigate the influence of thermal annealing on microstructure and mechanical properties and finally to map pathways

TABLE I. Results of microstructural and mechanical characterization of samples C1 and C2 in the as-prepared (as-prep.), relaxed, and coarse-grained (coarse) state: grain size $\langle D \rangle_{\text{vol}}$, bulk density ρ_{bulk}, elastic moduli G and B and Vickers hardness HV. The last line corresponds to a conventional $Pd_{90}Au_{10}$ sample solidified by arc melting and the values for G, B, and HV are taken from Ref. 30, where the theoretical density of 12.95 g/cm³ was used to calculate the elastic constants.

Sample	State	$\langle D \rangle_{\text{vol}}$ (nm)	ρ_{bulk} (g/cm³)	G (GPa)	B (GPa)	HV (GPa)
C1 (DSC)	As-prep.	10 (4)	12.07 (4)	35 (1)	129 (5)	3.34 (4)
C2 (DIL)	As-prep.	10 (3)	11.94 (4)	34 (1)	125 (5)	3.31 (5)
C1 (DSC)	Relaxed	12 (4)	12.33 (5)	38 (1)	152 (3)	4.17 (6)
C2 (DIL)	Relaxed	12 (3)	12.36 (5)	39 (1)	155 (2)	4.13 (4)
C1 (DSC)	Coarse	>10.000	12.58 (4)	…	…	2.46 (4)
C2 (DIL)	Coarse	>10.000	12.59 (4)	48 (2)	167 (12)	2.32 (5)
Reference	Solidified	>10.000	12.95	46 (2)	190 (18)	0.636 (6)

across the PEL, we examined two of the square pieces from the central section of the pellet. First, these two specimens named C1 and C2 were characterized in their as-prepared state regarding grain size, density, elastic constants, and Vickers hardness. The obtained results are summarized in Table I. In the next step, C1 was relaxed in the calorimeter (DSC) and C2 in the dilatometer (DIL). In both cases, the time–temperature protocol comprises a heating ramp from 20 °C to 117 °C with a nominal heating rate of 5 K/min and an isotherm at 117 °C for 98 h in the DIL and 12 h in the DSC, respectively. The different choice of relaxation times is owed to the higher sensitivity of the dilatometer (integral method) relative to the calorimeter (differential method), an issue that will be discussed in more detail later in this section. The recorded heat flux and irreversible length change are shown in Figs. 4(a) and 4(c), and the strain and enthalpy release are listed in Table II. After the relaxation, microstructure and mechanical properties of samples C1 and C2 were characterized again and the extracted results are also summarized in Table I.

To study the influence of grain growth on the material behavior, we heated both samples after relaxation to temperatures high enough to ensure that coarsening occurs.[41] This second annealing step was again performed in the DSC (sample C1) and the DIL (sample C2) and consisted of a heating ramp with a nominal heating rate of 5 K/min for 60 min. In this case, the time–temperature protocol was also carried out twice in the DIL, and the signal of the second measurement served as a reference to correct the thermal expansion of specimen C2 during continuous heating, so ensuring that only irreversible changes are considered. The specific heat flux and length change recorded during the high temperature annealing are shown in Figs. 4(b) and 4(d) together with the respective evolution of sample temperature. The corresponding strain and enthalpy release are listed in Table II. Finally, both samples were characterized again and the results are also included in Table I. An inspection of the microstructure by means of EBSD and OIM revealed grains in the order of several tens to hundreds of micrometers, confirming that grain growth engendered a coarse-grained polycrystalline microstructure.
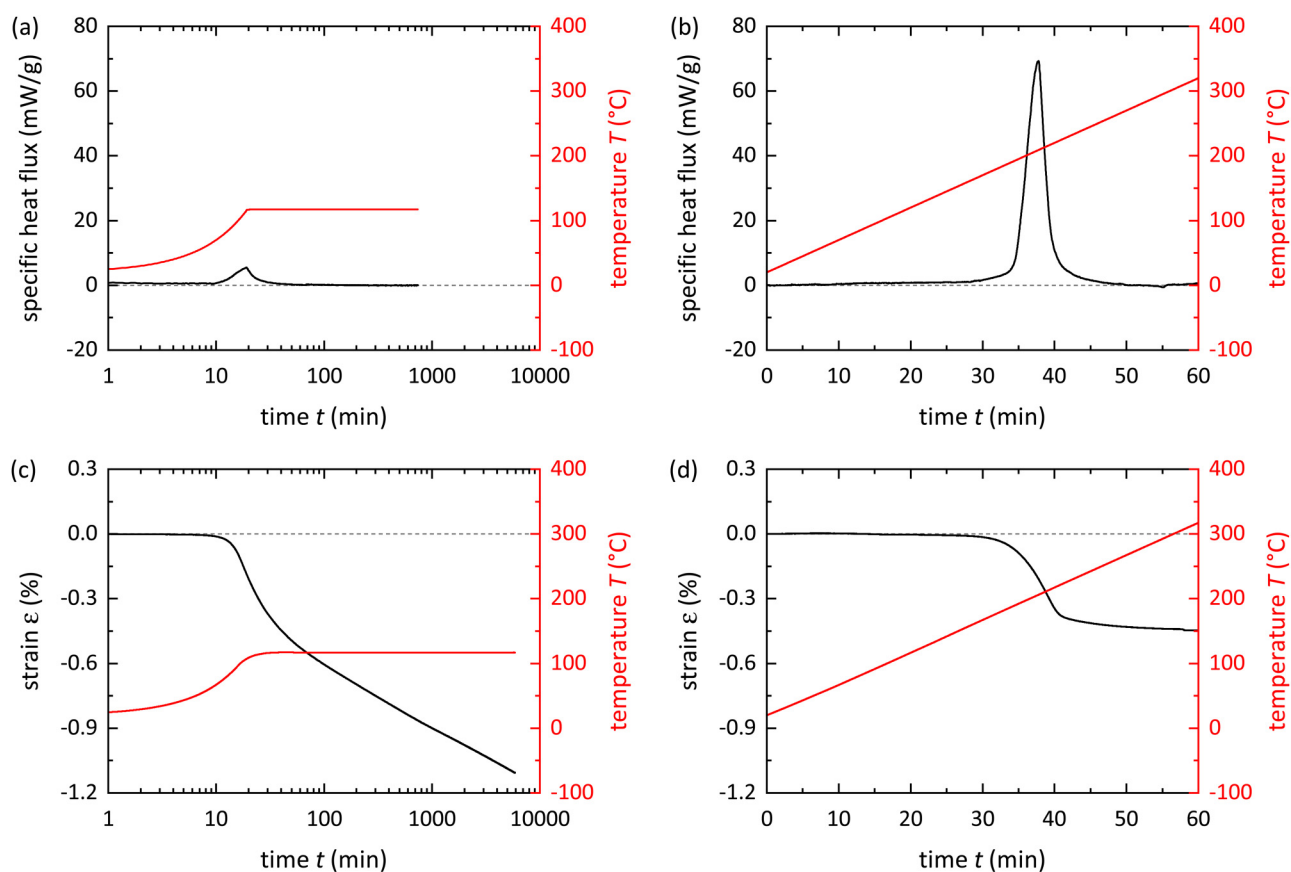
FIG. 4. Specific heat flux and length change induced by thermal annealing: specific heat flux recorded during (a) relaxation and (b) grain growth of specimen C1 and measured strain ε of sample C2 during (c) relaxation and (d) grain growth.

For comparison, the two other pieces cut from the center of the pellet were heated with a rate of 5 K/min for 60 min in the DSC (sample C3) and the DIL (sample C4) subsequent to the preparation process. The recorded strain and enthalpy release, including *both* relaxation and grain growth, are also listed in Table II. Furthermore, the microstructural and mechanical properties of a conventional coarse-grained sample of the same chemical

composition prepared by arc melting are reported as reference data in Table I.

A. Dilatometry and calorimetry

Before addressing the issue of reconstructing the PEL along the relaxation and grain growth path, it seems in order to discuss the recorded thermal, microstructural, and mechanical data sets in more detail. In the following, subscripts are used to denote properties in the as-prepared (ap), relaxed (rel), and coarse-grained (cg) state. Quantities that are assigned to a transition between two of these states are indicated by a subscript consisting of initial and final states separated by a right arrow.

Starting with the relaxation of specimen C1 in the calorimeter, we notice that the specific heat flux signal [Fig. 4(a)] shows only a detectable enthalpy release during the first hour of relaxation. In contrast, the length reduction of sample C2 in Fig. 4(c) does not saturate after isothermal annealing for 98 h at 117 °C. This finding can be understood when recalling that the DSC method detects the *rate* of enthalpy change (heat flux), which sets limits to the resolution of enthalpy change. As soon as the relaxation rate becomes so

TABLE II. Summary of strain ε and enthalpy ΔH releases during relaxation and grain growth of sample C1 and C2. The last row contains the results of the heating process performed on samples C3 and C4 including relaxation and grain growth. Furthermore, the corresponding change $\Delta\gamma_H$ or value of the grain boundary energy γ_H is tabulated.

Process	Sample	ε (%)	ΔH (J/g)	ΔH (meV/atom)	$\Delta\gamma_H$ or γ_H (J/m^2)
Relaxation	C1/C2	−1.11	2.95 (5)	3.5 (1)	$\Delta\gamma_H = 0.09$ (4)
Grain growth	C1/C2	−0.45	13.4 (5)	16.1 (1)	$\gamma_{H,\ rel} = 0.5$ (2)
Relaxation and grain growth	C3/C4	−1.4	19 (1)	22.8 (1)	$\gamma_{H,\ ap} = 0.9$ (2)

slow that it evades the sensitivity limit of heat flow detection, any change in enthalpy remains undetected even independent of the extent of the recoverable enthalpy.

Consequently, the enthalpy values extracted from DSC measurements manifest lower bound values for enthalpy release and hence enthalpy change associated with structural relaxation processes. The dilatometer, on the other hand, represents an integral measurement technique, which relies on measuring the evolution of absolute length and, therefore, integrating by design over all past length changes. Thus, DIL is perfectly adapted to study very slow, time-spread phenomena.

During the second annealing with a continuous heating rate, the recorded signals in Figs. 4(b) and 4(d) do not show any signature in the temperature range below 125 °C, where structural relaxation elapsed at basically constant grain size. Beyond 160 °C, however, we measure a length reduction accompanied by a simultaneous enthalpy release. Unlike above, this process entails a significant increase in grain size up to several tens or even hundreds of micrometers, which is equivalent to an almost complete annihilation of the overall GB area. We, therefore, conclude that the introduced two-stage annealing protocol enables studying structural relaxation behavior (almost) independent of grain growth.

The enthalpy releases induced by relaxation or by grain growth are determined by integrating the exothermic peaks of both processes in Figs. 4(a) and 4(b). The so acquired enthalpy values are included in Table II. Based on the observation that the grain size is practically constant during relaxation, we can use the corresponding enthalpy release $\Delta H_{\mathrm{ap}\to\mathrm{rel}}$ to calculate the change in the grain boundary energy $\Delta\gamma_{\mathrm{H}}$ associated with the relaxation of nonequilibrium GBs according to $\Delta\gamma_{\mathrm{H}} = \Delta H_{\mathrm{ap}\to\mathrm{rel}}/A_{\mathrm{GB,ap}} = 0.09\ (4)\ \mathrm{J/m^2}$.

We note that $\Delta H_{\mathrm{ap}\to\mathrm{rel}}$ and hence $\Delta\gamma_{\mathrm{H}}$ are lower bound values due to the above mentioned peculiarity of the DSC measurement method when applied to (very) slow relaxation processes. This restriction of measuring enthalpy changes is of fundamental nature. The only way of circumventing this restraint is by speeding up the relaxation dynamics and thereby increasing the heat flow. However, a straightforward prescription of how to enhance heat flow is missing since kinetic modeling of the relaxation behavior, discussed in detail in Paper I,[13] clearly demonstrated the absence of time–temperature superposition. It implies that the reduction of the relaxation time by increasing the temperature with the goal of reaching an equivalent enthalpy state does not obey a simple relation. More importantly, the range of available annealing temperatures should not exceed the temperature for the onset of grain growth, thus further limiting the achievable increase in heat flow.

The enthalpy release during grain growth $\Delta H_{\mathrm{rel}\to\mathrm{cg}}$ allows one to compute the GB energy of the relaxed boundaries $\gamma_{\mathrm{H,rel}} = \Delta H_{\mathrm{rel}\to\mathrm{cg}}/\Delta A_{\mathrm{GB}} = 0.5\ (2)\ \mathrm{J/m^2}$, where the accompanying change in GB area $\Delta A_{\mathrm{GB}} = A_{\mathrm{GB,rel}} - A_{\mathrm{GB,cg}}$ can be approximated by $\Delta A_{\mathrm{GB}} \approx A_{\mathrm{GB,rel}}$ for coarsening from $\approx 12\ \mathrm{nm}$ to grain sizes in the order of several tens to hundreds of micrometers. Due to the constantly increasing temperature [cf. Fig. 4(b)], grain growth occurs much less sluggishly than relaxation and so contributes to more accurate, although not quite as precise, values for $\Delta H_{\mathrm{rel}\to\mathrm{cg}}$ and $\gamma_{\mathrm{H,rel}}$.

Taking advantage of improved accuracy through continuously raising the temperature, an alternative way to determine $\Delta H_{\mathrm{ap}\to\mathrm{rel}}$

suggests itself, namely, by extracting $\Delta H_{\mathrm{ap}\to\mathrm{rel}}$ from the difference $\Delta H_{\mathrm{tot}} - \Delta H_{\mathrm{rel}\to\mathrm{cg}}$, where ΔH_{tot} represents the total enthalpy release associated with structural relaxation as well as grain growth. Continuously heating an *as-prepared* sample (sample C3) with a heating rate of $5\ \mathrm{K/min}$ for $60\ \mathrm{min}$ delivers the total enthalpy release ΔH_{tot}, also listed in Table II. As a result, we obtain $\Delta H_{\mathrm{ap}\to\mathrm{rel}} = 5.6\ \mathrm{J/g}$, a value which is significantly larger than the lower bound value of $2.95\ \mathrm{J/g}$ determined from only relaxing sample C1 (Table II). We conclude that $\Delta H_{\mathrm{ap}\to\mathrm{rel}} = 5.6\ \mathrm{J/g}$ more realistically reflects the highly nonequilibriated nature of the GB network in the as-prepared state. This assertion is also reflected by the computed value for $\gamma_{\mathrm{H,ap}} = \Delta H_{\mathrm{ap}\to\mathrm{cg}}/\Delta A_{\mathrm{GB,ap}} = 0.9\ (2)\ \mathrm{J/m^2}$, which is almost twice as large as $\gamma_{\mathrm{H,rel}} = 0.5\ (2)\ \mathrm{J/m^2}$.

Clearly, relaxation as well as grain growth correlate with a distinct length decrease represented by the evolution of negative irreversible strain over time. Two aspects are especially noteworthy: first, the strain evolution during relaxation does not yet seem to approach a steady state, although it is decelerating (note the logarithmic x-coordinate). Second, the strain caused by structural relaxation is much larger than that originating from grain growth. This finding suggests that the excess volume stored in the as-prepared state is not simply a consequence of the large GB area, but, in particular, reflects the nonequilibrium character (structural and energetic) of those GBs. Taking this assertion for granted, the observed evolution of negative strain during relaxation should manifest a one-dimensional signature of the depletion of the frozen-in positive volumetric strains or excess volume.[42,43] In fact, this claim can be directly tested by measuring the density ρ_{bulk} of samples C1 and C2 in the as-prepared, relaxed, and coarse-grained state so providing direct information on the content of free volume in the respective samples (see Table I). As a result, the bulk density increases during relaxation as well as grain growth, indicating a negative volume strain in both cases. In agreement with the DIL measurements, the density increase of 3.5% during relaxation is much larger than the increase of 1.9% caused by coarsening; the latter can be attributed to the nearly complete reduction of the grain boundary area.

Assuming that the material behaves perfectly isotropically so that the relative shrinkage through thermal annealing is identical in all three dimensions, one can also compute density changes based on the measured one-dimensional strains given in Table II. This results in a density increase of 3.4% for relaxation which compares favorably to a 3.5% increase measured by the Archimedes method, thus validating the assumption of statistical isotropy. As a matter of fact, strain isotropy is a characteristic feature of volume strain. On the other hand, we computed a density increase of 1.3% for grain growth by dilatometry compared to 1.9% by the Archimedes method, indicating that statistical isotropy is not strictly obeyed in this case. As a result, we, nevertheless, conclude that *structural relaxation* of IGC-prepared NC metals entails statistically isotropic changes of material properties.

We now pursue a contrasting juxtaposition of calorimetry (enthalpy/GB energy) and dilatometry (strain) data (cf. Fig. 4 and Table II). The most striking aspect of this juxtaposition is the observation that the larger length and volume reduction during relaxation ($\varepsilon = -1.11\%$) corresponds to the respective smaller enthalpy/GB energy change ($\Delta H_{\mathrm{ap}\to\mathrm{rel}} = 5.6\ \mathrm{J/g}$) and vice versa in the case of

grain growth ($\varepsilon = -0.45\%$ and $\Delta H_{\text{rel}\rightarrow\text{cg}} = 13.4\,\text{J/g}$). In other words, there is no simple correlation between change in energy and concomitant strain, as one might expect from, e.g., linear elasticity theory, where energy density is proportional to strain squared.

To reconcile this conflict, we argue that the material contains kinetically frozen-in nonequilibrium configurations, dominated by nonequilibrium GBs, which represent high energy inherent structures. Annealing provides the thermal energy to overcome the potential energy barriers, so driving the system toward equilibrium by virtue of relaxation and grain growth. This evolution entails local displacements and rearrangements of atoms on atomic length scales. The fact that relaxation as well as grain growth can be stopped practically instantaneously at any time by lowering the temperature suggests the existence of many closely spaced inherent-structure basins in a configuration space. This seems plausible since the count of distinguishable inherent structures Ω scales as $\ln(\Omega) \propto N$.[6] The puzzling evolution of strain and energy release discussed above can be reconciled by presuming that relaxation manifests relatively large macroscopical (negative) volume strains in conjunction with comparably small inter-basin energy differences. The opposite is true for grain growth.

As a corollary to the above reasoning, we recommend that volume strain is, in the present case, the most natural and accessible choice for a one-dimensional order parameter to describe the PEL. Obviously, a single order parameter is not able to fully capture the complex structural changes of the system during relaxation and/or grain growth, even at a macroscopic level. For example, volume preserving shear strains or mutually canceling local volume strains will not be probed by an overall volume strain. However, we are not aware of any better or complementing choice for an order parameter that relies on experimentally observable quantities.

Our goal of reconstructing an effective path through the PEL in terms of strain as order parameter requires information about barrier heights and basin/metabasin minima. We will demonstrate that the calorimetry data [cf. Figs. 4(a) and 4(b)] can be used to deduce the change in the enthalpies of the inherent structures along the relaxation and grain growth path. Likewise, we will show how the DIL data for relaxation and grain growth displayed in Figs. 4(c) and 4(d) allow one to extract the different barrier heights along the path as a function of strain release. We can take the analysis even a step further and estimate the change in the curvature of the bottoms of the basins. We first digress into this issue (Subsection IV B) to then proceed with the reconstruction of the PEL (Subsection IV C) based on the DSC and DIL data.

B. Elastic constants

We will present here a method to characterize the curvature of the bottoms of basins and its change with ongoing relaxation or grain growth. For that purpose, we simultaneously measured transverse and longitudinal ultrasonic velocities at room temperature in the as-prepared, relaxed, and coarse-grained state to compute the high frequency elastic moduli G and B (cf. Subsection III E and Table I). The ultrasound propagates as an elastic pulse in the limit of small amplitudes, hence small displacements and low energy, and so probes the state of the material *isoconfigurationally* and in the harmonic approximation for the vibrational dynamics. The central measurand

is the time delay between consecutive wide-band pulse echos, which is essentially the sum over all time delays over infinitesimal sections along the thickness of the sample. In fact, this is a further realization of an integral measurement method, which entails that the obtained moduli represent *effective* material properties.

The physics of elastic wave propagation is essentially determined by two different factors: the density of the material and the elastic constants C_{ijkl}, which relate to second derivatives (curvature) of the potential energy with respect to displacements. It follows that a traveling elastic wave generates time- and position-dependent three-dimensional strain. The propagation of this strain state depends on C_{ijkl}; we come back to this issue later.

By probing the material isoconfigurationally, its overall elastic behavior must reflect the statistically isotropic configuration,[44,45] which simplifies the problem of elastic wave propagation dramatically as the stiffness tensor is formed by only two independent quantities. Usually, the first and second Lamé constants $\lambda = C_{1122}$ and $\mu = 1/2(C_{1111} - C_{1122})$ are chosen, which allow for the compact representation $C_{ijkl} = \lambda \delta_{ij}\delta_{kl} + \mu(\delta_{ij}\delta_{kl} + \delta_{il}\delta_{jk})$. With this information, any elastic modulus (Young's modulus E, shear modulus G, bulk modulus B) or Poissons ratio ν can be computed. What remains to be clarified is the relation between elastic wave induced strain (fluctuations) and elastic moduli.

In general, any strain state represented by a second rank tensor $\bar{\bar{\varepsilon}}$ can be separated into an isotropic volume strain containing only identical diagonal elements $\varepsilon_{\text{vol}} = \text{Tr}(\bar{\bar{\varepsilon}})/3 = \sum_i \varepsilon_{ii}/3$ and the strain deviator $\bar{\bar{\varepsilon}}_{\text{dev}} = \bar{\bar{\varepsilon}} - \mathbb{1}\varepsilon_{\text{vol}}$, which describes pure shear without volume change which is responsible for any shape change of the observed sample.[46] It is straightforward to relate the shear modulus $G = \mu$ to volume conserving shear strain and associate the bulk modulus B with volume change. In other words, when deriving B and G from ultrasound measurements, we essentially extract data averaged over the entire specimen volume that hence reflect information about the mean curvature of the potential energy with respect to overall volume strains (order parameter), and shear strains, respectively. Specifically, for isotropic materials at constant temperature, the mean B and G moduli are related to the overall Helmholtz free energy F by[47]

$$B = \frac{1}{V}\frac{\partial^2 F}{\partial \varepsilon_{ii}^2} \quad \text{and} \quad G = \frac{1}{V}\frac{\partial^2 F}{\partial \varepsilon_{ij}^2}. \tag{4}$$

This implies that B and G are actually a direct measure of the curvature of Φ. For small deviations at the bottom of a basin, the volume depends linearly on ε_{ii}. Consequently, at constant pressure, the curvatures at the bottoms of corresponding Φ and $\Phi_{\text{H}} = \Phi + PV$ basins are identical because $\partial^2(PV)/\partial \varepsilon_{ii}^2 = 0$.

We further argue that the crystalline phase, although nanometer-sized, basically exhibits the same elastic constants as a conventional coarse-grained material of the same composition; they are a signature of the crystalline state. Deviations of the values of B and G from the coarse-grained reference are, therefore, attributed to the impact of the GB phase on the effective elastic moduli.[29] In addition to that, there is a porosity of $\simeq 3\%$, which is a characteristic feature of IGC-prepared samples[30] and has been validated to be basically constant during thermal annealing and so

does not affect relative changes between different states. In fact, after grain growth, the C samples exhibit a density deficit of 2.8% relative to the crystalline ground state.

We will now address the changes in B and G due to relaxation and grain growth. Both quantities are significantly lower in the NC states compared to their coarse-grained values, indicating the presence of the lower curvature at the bottom of the basin which is occupied by the system in the as-prepared state. Structural relaxation of sample C2 leads to an increase of G amounting to $G_{rel}/G_{ap} - 1$ is $\simeq 15\%$ and an even larger increase of B in the amount of $B_{rel}/B_{ap} - 1$ is $\simeq 24\%$; the changes in elastic constants affected by the relaxation of specimen C1 are smaller compared to C2 due to the shorter aging time in the DSC.

It should be noted that the density enters the calculation of both elastic moduli as a linear factor and thus contributes to their overall decrease in the NC state as well as to their relative increase during relaxation. However, this effect is proportional to the change in density which is only a minor contribution to the overall effect. For example, the density increases by only 3.5% during relaxation compared to a 24% increase in B.

Altogether, these findings yield clear-cut evidence that relaxation drives the system into basins with higher curvature. The different curvatures in the as-prepared, relaxed, coarse-grained and reference state are visualized in Fig. 5, where an atomic volume of $V = 14.94 \, \text{Å}^3$ was used to compute the local change ΔF of F in the near vicinity of the minima as a function of volume strain [cf. Eq. (4)]. The atomic volume was calculated by a linear rule of mixture from the atomic volumes of the pure elements listed in Ref. 48. What is more, the observed larger change in B compared to G let us conclude that the local curvature of the basins along the path toward lower energy becomes more narrow with respect to volumetric strains compared to shear strains.

C. Energy landscape

Referring to the above presented results, we are now prepared to describe the path across the PEL—as it has been taken by our samples during relaxation and grain growth—in terms of volumetric strain and energy. We divide this task into two main parts: first, the reconstruction of the inherent-structure enthalpy differences, and second, we present a rationale of how to retrieve the effective barrier heights the system must overcome on its path to global equilibrium. We will address these issues separately and eventually combine the information to draw a picture of the PEL.

Reconstruction of the energy minima the system passes through is directly related to the results gained from the DSC measurements (cf. Sec. II). In particular, the measured enthalpy differences between the as-prepared, relaxed, and coarse-grained state, respectively, (see Table II) set the landmarks of enthalpy release of the system on its path to equilibrium (cf. Fig. 6). Since only enthalpy differences are physically relevant, we are free to prescribe a reference value of enthalpy for a particular state. We select the coarse-grained state and assign a value of 0.005 eV/atom to it since we prefer to display energy values also on a log scale, which forbids stipulating zero enthalpy.

The release of enthalpy between the as-prepared and relaxed state—before the onset of grain growth—manifests the driving force for the relaxation dynamics. The associated sequence of energy minima can be inferred from the DSC measurement [cf. Fig. 4(a)] by integrating the specific heat flux with respect to
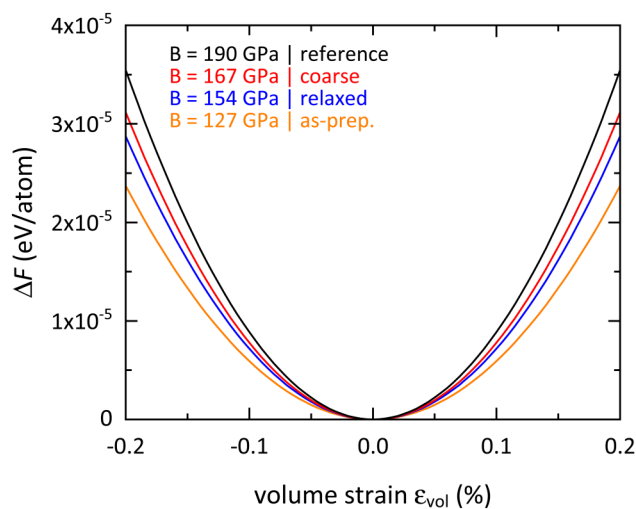

FIG. 5. Increase in free energy ΔF due to volume strain ε_{vol} measured relative to the potential energy minimum of different inherent structures representing different material states: the as-prepared (as-prep.), relaxed, coarse-grained (coarse), as well as the arc-melted reference state. The different curvatures related to the different sample states correspond to different bulk moduli B which are listed in Table I. In the case of the as-prepared and relaxed state, the mean value of samples C1 and C2 is plotted in the diagram.
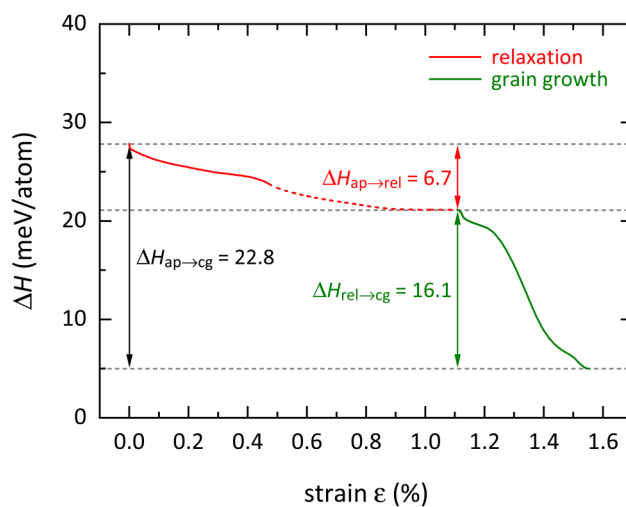

FIG. 6. Energy minima of the potential energy landscape along the relaxation and grain growth path as a function of strain ε probed by means of enthalpy differences ΔH with reference to the coarse-grained ground state (bottom dashed horizontal line). The vertical double arrows indicate the enthalpy differences reported in Table II. The full red and full green curve shapes are extracted from the recorded DSC-data (Fig. 4). The dashed red line bridges a gap of missing data and relies on a extrapolation scheme. For more details, we refer to the text.

time. However, we face the problem here that at around 40 min the DSC method approaches its resolution limit, as discussed in detail in Subsection IV A, although enthalpy and strain release [cf. Fig. 4(c)] *de facto* proceed.

Obviously, we are confronted by a gap of missing data for the evolution of enthalpy release with time. It opens up at strain values of $\approx -0.5\%$ at around 40 min [cf. Figs. 4(a) and 4(c)] and extends to $\approx -1.1\%$ at around 6000 min before the onset of grain growth (cf. Table II). To bridge this gap, physical reasoning requires that the prevailing non-zero specific heat flux must be approximated by a continuous and decreasing function with concave-up curvature to provide for the decelerating kinetics of structural relaxation. Analyzing the release of heat flux along the isothermal annealing segment [cf. Fig. 4(a)], we found that a sum of three exponential decay functions fitted the data best. We used these exponentials to extrapolate the so approximated heat flux data to increasing strain/time values up to the onset of grain growth. The resulting evolution of enthalpy release and hence the sequence of enthalpy minima along the path is displayed as dashed red line in Fig. 6.

The transition from the relaxed to the coarse-grained state develops through grain growth. It is accompanied by a much more pronounced heat flux signal compared to relaxation. We make direct use of the integrated heat flux—resolution problems are negligible here—to deduce the sequence of enthalpy minima which continuously link the relaxed to the coarse-grained state. The entire sequence together with the enthalpy differences reported in Table II are shown in Fig. 6.

Regarding numbers, we note that $\Delta H_{ap \to rel} = 6.7$ meV/atom or 5.6 J/g (see Fig. 6 and Sec. IV A) is in the order of magnitude comparable with $k_B T$ at room temperature. This finding is compatible with data obtained by computer simulations that investigated aging and rejuvenation phenomena in terms of excitations in the potential energy landscape.[49] Likewise, rapidly quenched (melt-spun) metallic glasses exhibit significant excess enthalpy when heated to the glass transition temperature in a calorimeter. The so explored range of heat of relaxation ΔH_{rel} varied between 11% and 17% of the enthalpy of melting ΔH_m ($1 - 1.5$ kJ/mol) as *representative* values.[9,50] Assuming a linear rule of mixture value of $\Delta H_m = 16.3$ kJ/mol for the enthalpy of melting of the fully miscible $Pd_{90}Au_{10}$ alloy,[51] we estimate for 14% of ΔH_m a related value of $\Delta H_{rel} = \Delta H_{ap \to rel} \approx 20$ J/g, which is about four times larger than our finding $\Delta H_{ap \to rel} = 5.6$ J/g. However, one has to consider that the microstructure of both materials is quite different. Short- and medium-range disorder in metallic glasses prevails more or less homogeneously across the volume. On the contrary, atomic site disorder in NC metals is predominantly localized in the core region of GBs, whereas the atoms in the abutting crystallites are arranged on lattice sites. Knowing the average grain size $\langle D \rangle_{vol}$, the width of the grain size distribution $\sigma = 1.7$,[34] as well as assuming an average thickness of the GBs of $\delta = 1$ nm,[29] it is straightforward to compute the volume fraction of atoms located in the core region of GBs according to Eq. (A5). With the grain size of $\langle D \rangle_{vol} = 10(4)$ nm (cf. Table I), the volume fraction of GB atoms varies between 40% and 22%. If we attribute the measured ΔH_{rel} to the share of GB atoms, we find 14 J/g $< \Delta H_{rel} <$ 25 J/g, a relation that is no longer in conflict with $\Delta H_{rel} = 0.14 \Delta H_m$.

We continue by addressing the issue of potential barriers between adjacent energy minima. Since barrier heights relate to activation energies between initial and final states, it appears advantageous to first digress into Paper I[13] that is just concerned with this issue. The focus of this work relates to the kinetics of volume/strain relaxation in NC $Pd_{90}Au_{10}$ and, in particular, deals with *modeling* of strain relaxation data obtained from dilatometry in terms of a distributed reactivity model.[52] It partitions the overall process into a set of independent and parallel reactions i, each of which is characterized by a triplet of activation parameters: Gibbs free energies of activation ΔG_i^*, maximum possible strain contribution $\varepsilon_{max,i}$ of process i to the overall strain, and the high temperature strain rate limit $\dot{\varepsilon}_{max,i}$. These parameters enter Eq. (5), which is the fundamental differential equation underlying the distributed reactivity model. To demonstrate the validity of this model, we apply it to the DIL data shown in Fig. 4(c). The fit to the DIL data is shown in Fig. 7(a), and the underlying activation parameters are
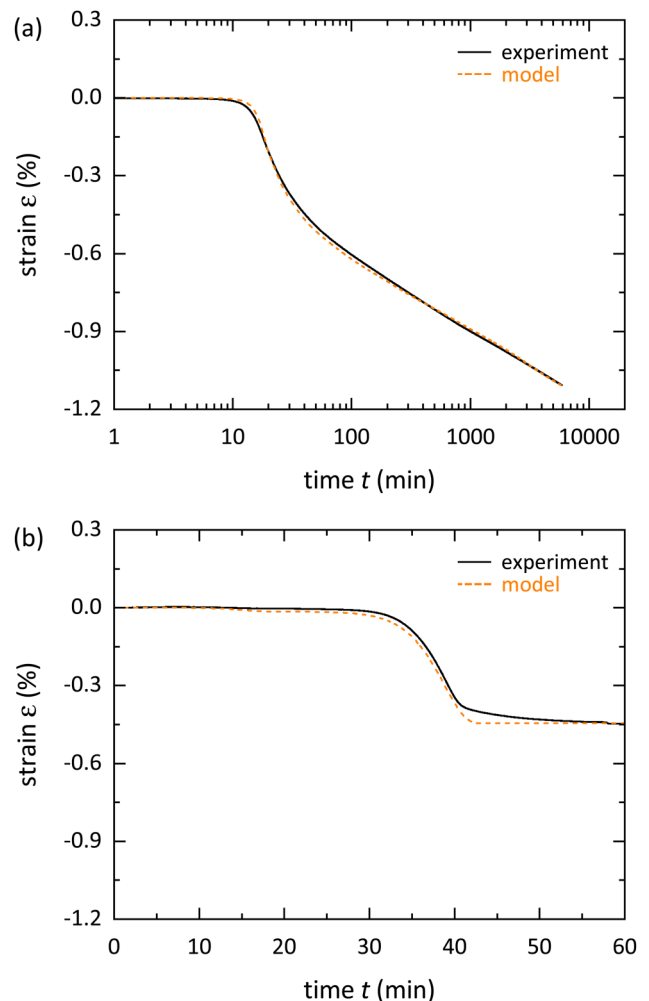

FIG. 7. Time evolution of measured (experiment) and modeled strain during (a) relaxation and (b) grain growth of sample C2.

TABLE III. Kinetic parameters of sample C2 for relaxation. $\Delta G_i^\star$ denotes the Gibbs free energies of activation, $\varepsilon_{\max,i}$ is the maximum possible strain contribution of process i to the overall strain, and $\dot{\varepsilon}_{\max,i}$ is the high temperature strain rate limit.

Process i	$\Delta G_i^\star$ (eV)	$\varepsilon_{\max,i}$ (%)	$\dot{\varepsilon}_{\max,i}$ (10^8/s)
1	0.950 (1)	−0.134	−1.94
2	0.991 (1)	−0.134	−1.94
3	1.033 (1)	−0.134	−1.94
4	1.074 (2)	−0.134	−1.94
5	1.116 (2)	−0.134	−1.94
6	1.157 (3)	−0.134	−1.94
7	1.20 (1)	−0.200	−1.94
8	1.24 (2)	−0.200	−1.94

reported in Table III. For the sake of convenience and with regard to further analysis, we restricted $\dot{\varepsilon}_{\max,i}$ to an average value of $\langle \dot{\varepsilon}_{\max,i} \rangle = -1.94 \times 10^8$ 1/s, chose equidistantly distributed free energies of activation, and restricted $\varepsilon_{\max,i}$ to only two representative values; this simplified thermal parameter variation is directly derived from the results in Ref. 13 on the same material.

Since kinetic analysis is not restricted to a specific process, we analyzed the grain growth data obtained by DIL in an analogous manner. The most simple viable model consists of a set of only two parallel reactions (cf. Table IV) as shown in Fig. 7(b). The process $i = 1$ is characterized by a minute maximum possible strain contribution $\varepsilon_{\max,1} = -0.015\,\%$ and a comparatively small Gibbs free energy of activation $\Delta G_1^\star = 0.935$ eV (cf. Table III). We suggest that process $i = 1$ reflects a residual relaxation after reheating the sample. We suppose that the relatively fast cooling of the sample subsequent to aging without appreciable grain growth did not enable the material to reach the minimum of the metabasin. Hence, reheating the sample in the temperature range below the onset of significant grain growth initially supplies sufficient energy to make the material relax within the metabasin to assume minimal energy.

The process $i = 2$ represents the subsequent grain growth at higher temperatures[41] which necessarily involves the escape of the system from the metabasin. It should be noted that it is impossible to guarantee that process $i = 2$ represents at every point in time exclusively an increase in the average grain size. In fact, in each time increment, a certain amount of process $i = 2$ might be attributed to grain size preserving relaxation processes. We note that the kinetics of grain growth commonly involves a mobility term that entails a single apparent activation energy[53] well in agreement with our simplified analysis.

TABLE IV. Kinetic parameters of sample C2 for grain growth. $\Delta G_i^\star$ denotes Gibbs free energies of activation, $\varepsilon_{\max,i}$ is the maximum possible strain contribution of process i to the overall strain, and $\dot{\varepsilon}_{\max,i}$ is the high temperature strain rate limit.

Process i	$\Delta G_i^\star$ (eV)	$\varepsilon_{\max,i}$ (%)	$\dot{\varepsilon}_{\max,i}$ (10^8/s)
1	0.935 (1)	−0.015	−0.33
2	1.25 (2)	−0.430	−7.60

What remains to be done is deriving, based on the distinct free energies of activation (cf. Tables III and IV), an expression for the barrier heights $\Delta G_{\mathrm{eff}}^\star$ as a function of time and hence strain (cf. Fig. 7). In other words, we need a diagram for the effective barrier height in full analogy to the graph of the effective energy minima displayed in Fig. 6. To achieve this goal, it is essential to start off with the fundamental differential equation of the distributed reactivity model which is formulated in terms of strain rate $d\varepsilon/dt$ and reads

$$\frac{d\varepsilon}{dt} = \sum_{i=1}^{n} k_i(T(t)) f_i(\varepsilon_i(t)). \tag{5}$$

The independent and parallel reactions i are expressed as the products of an Arrhenius expression $k_i(T(t)) = \dot{\varepsilon}_{0,i}(T(t))\exp(-\Delta G_i^\star/k_B T(t))$ and a reaction model $f_i(\varepsilon_i(t))$, where $T(t)$ represents the given time–temperature protocol; for more details of the model, we refer to Ref. 13.

We argue that for sufficiently small time intervals, the structural relaxation kinetics can be modeled by a single step process. As a consequence, Eq. (5) simplifies to the conventional Arrhenius ansatz

$$\frac{d\varepsilon}{dt} = \dot{\varepsilon}_0 \exp\left(-\frac{\Delta G_{\mathrm{eff}}^\star}{k_B T}\right), \tag{6}$$

where all symbols have their usual meaning. Equating Eq. (6) with Eq. (5) for each time interval Δt and solving for $\Delta G_{\mathrm{eff}}^\star$ gives the sought relation for the *effective barrier height* at time t, $\Delta G_{\mathrm{eff}}^\star(t)$, as

$$\Delta G_{\mathrm{eff}}^\star(t) = -k_B T \ln\left(\frac{1}{\dot{\varepsilon}_0} \sum_i k_i(T(t)) f_i(\varepsilon_i(t))\right), \tag{7}$$

which can be solved numerically by setting $\dot{\varepsilon}_0 = \langle \dot{\varepsilon}_{\max,i} \rangle$ and using the activation parameters from Table III for structural relaxation. The effective barrier heights for grain growth are computed along the same line of reasoning but based on Table IV.

Referring to Fig. 7, it is straightforward to transform $\Delta G_{\mathrm{eff}}^\star(t)$ [cf. Eq. (7)] into $\Delta G_{\mathrm{eff}}^\star(\varepsilon)$, which is depicted in Fig. 8. Structural relaxation is modeled by 25 000 time intervals and grain growth by 15 000. These numbers reflect the temporal resolution of the modeling. This is the fundamental reason, why all presented values for $\Delta G_{\mathrm{eff}}^\star(t)$ and $\Delta H(t)$ are effective values averaged over technically required time intervals. They should not be confused with the much higher actual number of basins and saddle points along the path across the PEL. Structural relaxation exhibits a continuous increase in $\Delta G_{\mathrm{eff}}^\star(\varepsilon)$ with strain/time, which reflects the depletion of relaxation processes with low activation barrier. With regard to grain growth, $\Delta G_{\mathrm{eff}}^\star(\varepsilon)$ is mostly constant with the exception of a jump discontinuity observed at the crossover from relaxation to grain growth. This discontinuity is presumably caused by the previously discussed relaxation after reheating the sample.

The central result of this work which imparts the inherent-structure enthalpies and barrier heights along the path across the PEL is shown in Fig. 9. The characteristic feature of this landscape is reflected by the large height of energy barriers (>1 eV/atom)
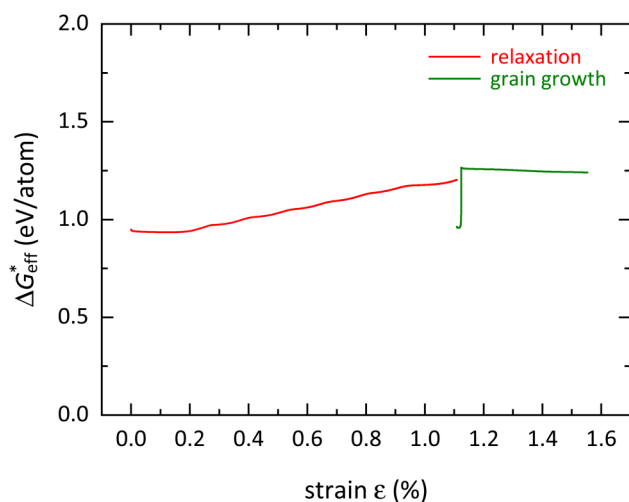
FIG. 8. Effective barrier height $\Delta G^*_{eff}(\varepsilon)$ as a function of strain ε. The jump discontinuity observed at the crossover from relaxation to grain growth is caused by a residual relaxation after reheating the sample; for more details, we refer to the text.

compared to the small differences between successive inherent-structure enthalpies. As a consequence, the relaxation dynamics at typical annealing temperatures should be relatively slow. The experiments carried out so far are not covering long-time ($>10^5$ min) relaxation dynamics, therefore, we may miss processes having relatively large residence times in their related basins. The finite slope of strain release after 10^4 min of annealing time [cf. Fig. 4(c)] is
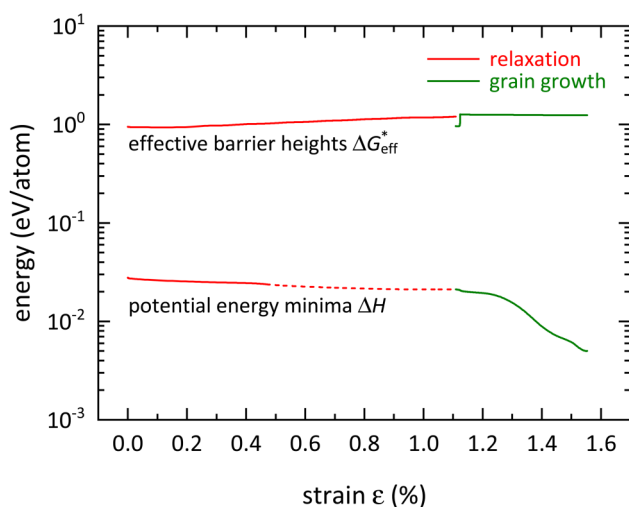

FIG. 9. Effective barrier height $\Delta G^*_{eff}(\varepsilon)$ and energy minima of the PEL probed by enthalpy differences $\Delta H(\varepsilon)$ along the path across the PEL as a function of strain ε.

indicative of still ongoing long-time processes not yet covered by our analysis. Furthermore, our results show that with ongoing relaxation or grain growth, the inter-basin energy difference becomes smaller, while the barrier height becomes larger. This causes a deceleration of the dynamics driving the system toward global equilibrium, or in other words, the system behaves as a bad/slow global minimum finder.[54]

Finally, we shortly demonstrate that the relaxed material state not only manifests property changes compared to the as-prepared as well as the reference state but even reveals considerably enhanced properties.

D. Deformation behavior

We investigated the macroscopic deformation behavior of the different sample states to find out to which extent relaxation and grain growth go along with mechanical property changes. In Fig. 10, we display Vickers indentations obtained from as-prepared, relaxed, and coarse-grained samples. The square of the length of the diagonals of the indents is inversely proportional to hardness, which correlates with yield stress or ultimate tensile strength in the case of ductile materials. Technically, the increasing penetration of the tip into the material at a constant load goes along with a continuous decrease of the applied stress due to the continuously increasing indentation surface. If the so applied stress drops below the yield stress plastic deformation ceases, hence rendering the diagonal of the indent a direct measure of the yield stress. As can be gathered from Table I, the hardness of the NC materials in its as-prepared state (HV ≈ 3.33 GPa) is approximately five times larger than the reference sample prepared by the solidification of the molten $Pd_{90}Au_{10}$ alloy (HV ≈ 0.64 GPa). The slogan "smaller is stronger" certainly applies to the as-prepared material state in agreement with what is expected for NC materials at the low end of the nanoscale. A striking finding relates to the continued 25% increase of hardness associated with structural relaxation of the as-prepared material; *relaxation hardening*[55] amounts to HV values of HV ≈ 4.15 GPa.

The SEM micrograph of the indented as-prepared sample [Fig. 10(a)] do not show any indications of volume preserving deformation that typically creates material pileup at the edges of indentation usually observed in this alloy [Fig. 10(c)]. It appears that the high initially applied stress leads to stress-driven relaxation with concomitant annihilation of excess volume along with consolidation (densification) in the sample volume below the indenter. This volume seems to carry the deformation until the diminishing applied stress neither causes appreciable relaxation nor plastic deformation.

The relaxed sample [Fig. 10(b)] exhibits a similar behavior. Again, pileup is basically missing. We conjecture that the very high initial stress under the indenter tip still activates stress-driven relaxation along with plastic deformation causing consolidation in the volume below the indent; albeit to a lesser extent compared to the as-prepared sample, resulting in a smaller indent. Such behavior reflects the reduced potential for further relaxation of the relaxed sample vs the as-prepared one. This finding agrees with our previous result revealing that barrier heights increase during relaxation thus suggesting that higher stresses are required for further
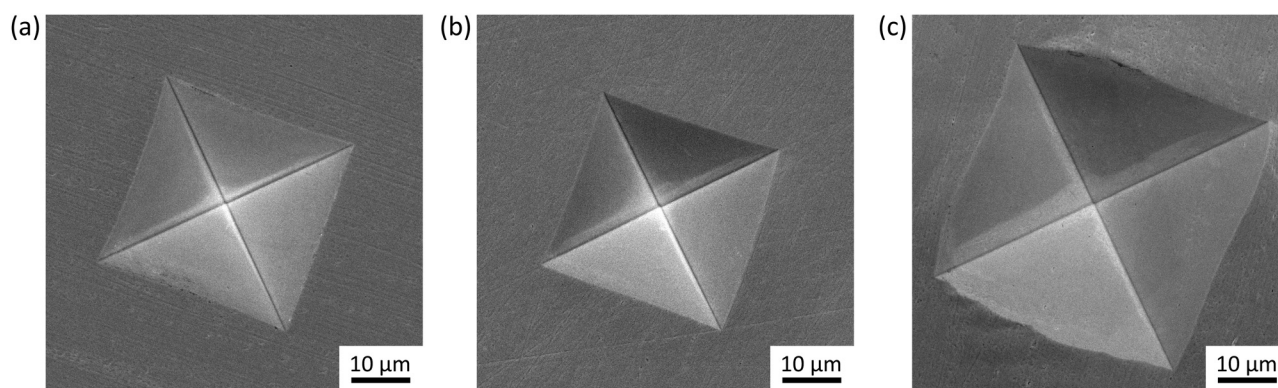
FIG. 10. SEM images of HV0.5 indents in the (a) as-prepared, (b) relaxed, and (c) coarse-grained state.

relaxation in already relaxed samples. Finally, we note that the indentations in Fig. 10 were taken with a five times higher load (HV 0.5) compared to the hardness values (HV 0.1) displayed in Table I. As expected, the respective extracted hardness values agree; however, morphological details can be much better resolved for larger indent sizes.

Surprisingly, annealing of the relaxed samples and concomitant grain growth indeed involves the formation of micrometer-sized grains ($>10\,\mu m$); however, the hardness remains still much larger than expected. In fact, the so prepared coarse-grained state exhibits a hardness of HV ≈ 2.4 GPa that is still a factor of 3.75 larger than the hardness of the solidified polycrystal with a comparable grain size. Further work is needed to scrutinize this effect. Nevertheless, it seems likely to assume that characteristics of the PEL prevent the system from straightforwardly approaching global equilibrium.

The observation that the deformation behavior depends on the specific sample states seems to be reflected by the increasing B/G ratio that amounts to 3.7(2) in the as-prepared state and assumes a value of 4.0(2) after structural relaxation. The B/G ratio is in contrast to the individual elastic constants independent of sample density and only related to the transversal and longitudinal sound velocities.[56,57] We recall that the B/G ratio has been introduced into the literature in the fifties of the last century to distinguish between ductile ($B/G \gtrsim 2.3$) or brittle behavior of polycrystalline fcc metals.[58] The rationale behind this criterion was solely based on dislocation emission and glide.[59,60] Interestingly, the value of 4.0(2) we find for the relaxed state perfectly agrees with theory values, $B/G = 3.99$, for the statistically isotropic and homogeneous polycrystal.[61] Hence, it is implied that relaxation equilibrates the highly nonequilibrated GBs which prevail in the as-prepared state.

The metallic glass community could demonstrate that the B/G criterion is also applicable to categorize metallic glasses. In fact, it can be shown that the B/G ratio is cardinal to any metallically bonded system.[62,63] Moreover, B/G scales inversely to the so-called non-ergodicity parameter f_0, which has been introduced to quantify the amplitude of density fluctuations in metallic glasses.[56,57] In other words, the observed increase of B/G during relaxation is

then indicative of decreasing density fluctuations, which should manifest the transition from nonequilibrium to equilibrium GBs and thus quite independently agrees with the findings and reasoning of this work.

V. SUMMARY AND CONCLUSIONS

Amorphous and nanostructured materials are commonly not in equilibrium relative to the laboratory time scale. As a consequence, their thermodynamic, dynamic, and physical properties change with time, a behavior that has been termed aging or structural relaxation.[1,2] The microscopic processes which manifest the systems structural relaxation dynamics toward equilibrium go along with configurational changes in the system. Such changes are accompanied by an evolution of state variables, e.g., volume and enthalpy, and concomitantly alter physical properties. Behavior like that is a manifestation of the underlying potential energy landscape (PEL), which is a complex $3N$-dimensional hypersurface in a $(3N+1)$-dimensional space.[3,5,6,64]

In order to gain insight and even predict how properties change in the course of aging, it is crucial to establish their relation to the PEL. In general, this is a formidable task. To, nevertheless, handle the problem, one-dimensional representations of potential energy functions are usually constructed.[5] They require information about local energy minima as well as transition states (saddle points) and how they relate to a one-dimensional order parameter.

In this work, we studied the structural relaxation of nanocrystalline $Pd_{90}Au_{10}$ and exploited strain/volume release as an order parameter. We used calorimetry to retrieve how energy/enthalpy of relative minima evolves when the system crosses transition states on its way to global equilibrium. In Paper I,[13] we studied in great detail how the spectrum of effective barrier heights—which the system must overcome to reach equilibrium—can be extracted from dilatometry. Here, we applied this method to map out the spectrum of barrier hights.

With this information, it became feasible to reconstruct the *effective* inherent-structure enthalpies and barrier heights along a

path across the PEL in terms of volume strain as our order parameter (see Fig. 9). Volume conserving shear–strain contributions are thereby neglected. The characteristic feature of this landscape is reflected by the large height of energy barriers (>1 eV/atom) compared to the energy difference between adjacent minima ($<k_B T$ at room temperature), thus identifying this system as a bad global minimum finder.

In conclusion, we demonstrated that structural relaxation and grain growth go along with significant property changes. We studied hardness (cf. Fig. 10) to find pronounced relaxation hardening.[55] The hardness values that emerge after grain growth (grain size $>10\,\mu$m) are surprisingly large (≈ 2.4 GPa) compared to the solidified polycrystalline reference material (≈ 0.64 GPa), clearly indicating a consequence of the discussed landscape and its nature of being a bad global minimum finder. Moreover, we extracted a decrease of the non-ergodicity parameter f_0,[56,57] which scales inversely to B/G. The observed decrease of f_0 is indicative of decreasing density fluctuations, which we mainly attribute to a transition from nonequilibrium to equilibrium grain boundaries with advancing relaxation. This reasoning is quite independently consistent with the findings derived from the sequence of inherent structures along the path across the PEL.

ACKNOWLEDGMENTS

APPENDIX: GRAIN BOUNDARY VOLUME FRACTION

For the sake of simplicity, we assume spherical grains with grain diameters D following a lognormal distribution $g(D)$, which is usually determined by the median of grain diameter D_0 and a distribution width parameter σ. In this work, grain size is characterized through x-ray diffraction by the volume-weighted average grain diameter $\langle D \rangle_{\text{vol}}$, which is obtained as the 4th moment of the distribution divided by the 3rd.[34] The median D_0 can be expressed by $\langle D \rangle_{\text{vol}}$ and σ as

$$D_0 = \langle D \rangle_{\text{vol}} \exp\left(-\frac{7}{2} \ln^2 (\sigma) \right). \tag{A1}$$

Thus, the lognormal distribution assumes the form

$$g(D) = \frac{1}{\sqrt{2\pi} D \ln (\sigma)} \exp\left(-\frac{\ln^2 (D/D_0)}{2 \ln^2 (\sigma)} \right). \tag{A2}$$

If we assign an average thickness δ to the GBs, each individual grain is connected with a share of the GB thickness of $\delta/2$. The volume share of the GB of a single grain is the volume of the GB, V_{GB}, divided by the total volume V, which is for a spherical grain

$$\frac{V_{\text{GB}}(D)}{V(D)} = \frac{\frac{4}{3}\pi \left(\left(\frac{D}{2} + \frac{\delta}{2} \right)^3 - \left(\frac{D}{2} \right)^3 \right)}{\frac{4}{3}\pi \left(\frac{D}{2} + \frac{\delta}{2} \right)^3}. \tag{A3}$$

For NC samples with grain sizes following the lognormal distribution, the GB volume share becomes

$$\frac{V_{\text{GB}}}{V} = \frac{\int_{D=0}^{\infty} g(D) V_{\text{GB}}(D) \mathrm{d}D}{\int_{D=0}^{\infty} g(D) V(D) \mathrm{d}D} \tag{A4}$$

$$= \frac{3\delta}{3\delta + \exp\left(\ln\left(\langle D \rangle_{\text{vol}} \right) - \ln^2 (\sigma) \right)}. \tag{A5}$$

REFERENCES

[1]L. C. E. Struik, *Physical Aging in Amorphous Polymers and Other Materials* (Elsevier Scientific Publishing Company, 1978).

[2]I. M. Hodge, "Enthalpy relaxation and recovery in amorphous materials," J. NonCryst. Solids **169**, 211–266 (1994).

[3]M. Goldstein, "Viscous liquids and the glass transition: A potential energy barrier picture," J. Chem. Phys. **51**, 3728–3739 (1969).

[4]F. H. Stillinger and T. A. Weber, "Hidden structure in liquids," Phys. Rev. A **25**, 978–989 (1982).

[5]D. J. Wales, *Energy Landscapes: Applications to Clusters, Biomolecules and Glasses*, Cambridge Molecular Science (Cambridge University Press, 2004).

[6]F. H. Stillinger, *Energy Landscapes, Inherent Structures, and Condensed-Matter Phenomena* (Princeton University Press, 2015).

[7]F. H. Stillinger, "A topographic view of supercooled liquids and glass formation," Science **267**, 1935–1939 (1995).

[8]A. Heuer, "Exploring the potential energy landscape of glass-forming systems: From inherent structures via metabasins to macroscopic transport," J. Phys. Condens. Matter **20**, 373101 (2008).

[9]Y. Sun, A. Concustell, and A. L. Greer, "Thermomechanical processing of metallic glasses: Extending the range of the glassy state," Nat. Rev. Mater. **1**, 16039 (2016).

[10]V. Lubchenko and P. G. Wolynes, "Theory of aging in structural glasses," J. Chem. Phys. **121**, 2852–2865 (2004).

[11]S. K. S. Mazinani and R. Richert, "Enthalpy recovery in glassy materials: Heterogeneous versus homogenous models," J. Chem. Phys. **136**, 174515 (2012).

[12]E. Donth, *The Glass Transition: Relaxation Dynamics in Liquids and Disordered Materials*, Springer Series in Materials Science Vol. 48 (Springer, Berlin, 2001).

[13]M. J. Deckarm, C. Braun, and R. Birringer, "Structural relaxation of nanocrystalline PdAu alloy: Probing the spectrum of potential barriers," J. Appl. Phys. **126**, 205102 (2019).

[14]C. A. Angell, K. L. Ngai, G. B. McKenna, P. F. McMillan, and S. W. Martin, "Relaxation in glassforming liquids and amorphous solids," J. Appl. Phys. **88**, 3113–3157 (2000).

[15]H. Gleiter, "Nanostructured materials: Basic concepts and microstructure," Acta Mater. **48**, 1–29 (2000).

[16]R. Birringer, "Nanocrystalline materials," Mater. Sci. Eng. A **117**, 33–43 (1989).

[17]R. Z. Valiev, R. K. Islamgaliev, and I. V. Alexandrov, "Bulk nanostructured materials from severe plastic deformation," Prog. Mater. Sci. **45**, 103–189 (2000).

[18]A. Tschöpe and R. Birringer, "Thermodynamics of nanocrystalline platinum," Acta Metall. Mater. **41**, 2791–2796 (1993).

[19]A. Tschöpe, R. Birringer, and H. Gleiter, "Calorimetric measurements of the thermal relaxation in nanocrystalline platinum," J. Appl. Phys. **71**, 5391–5394 (1992).

[20]M. Atzmon and J. D. Ju, "Microscopic description of flow defects and relaxation in metallic glasses," Phys. Rev. E **90**, 042313 (2014).

21 M. Ames, J. Markmann, R. Karos, A. Michels, A. Tschöpe, and R. Birringer, "Unraveling the nature of room temperature grain growth in nanocrystalline materials," Acta Mater. **56**, 4255–4266 (2008).

22 A. Michels, C. E. Krill, H. Ehrhardt, R. Birringer, and D. T. Wu, "Modelling the influence of grain-size-dependent solute drag on the kinetics of grain growth in nanocrystalline materials," Acta Mater. **47**, 2143–2152 (1999).

23 R. Kohlrausch, "Theorie des elektrischen Rückstandes in der Leidener Flasche," Annal. Physik Chem. **91**, 56–82 (1854).

24 M. Atzmon, "The pitfalls of empirical fitting of glass relaxation data with stretched exponents," J. Appl. Phys. **123**, 065103 (2018).

25 H. B. Callen, *Thermodynamics and an Introduction to Thermostatics*, 2nd ed. (John Wiley & Sons, 1985).

26 R. Birringer, "Structure of nanostructured materials," in *Nanophase Materials*, NATO ASI Series (Series E: Applied Sciences), edited by G. C. Hadjipanayis and R. W. Siegel Vol. 260 (Springer, Dordrecht, 1994), pp. 157–180.

27 A. P. Sutton and R. W. Balluffi, *Interfaces in Crystalline Materials*, Oxford Classic Texts in the Physical Sciences (Oxford University Press, Oxford, 2006).

28 J. M. Howe, *Interfaces in Materials* (John Wiley & Sons, 1997).

29 M. Grewer, J. Markmann, R. Karos, W. Arnold, and R. Birringer, "Shear softening of grain boundaries in nanocrystalline Pd," Acta Mater. **59**, 1523–1529 (2011).

30 A. Leibner, C. Braun, J. Heppe, M. Grewer, and R. Birringer, "Plastic yielding in nanocrystalline Pd-Au alloys mimics universal behavior of metallic glasses," Phys. Rev. B **91**, 174110 (2015).

31 A. Stukowski, J. Markmann, J. Weissmüller, and K. Albe, "Atomistic origin of microstrain broadening in diffraction data of nanocrystalline solids," Acta Mater. **57**, 1648–1654 (2009).

32 A. Leonardi, M. Leoni, and P. Scardi, "Atomistic interpretation of microstrain in diffraction line profile analysis," Thin Solid Films **530**, 40–43 (2013).

33 R. Birringer, M. Hoffmann, and P. Zimmer, "Interface stress in nanocrystalline materials," Z. Metall. **94**, 1052–1061 (2003).

34 C. E. Krill and R. Birringer, "Estimating grain-size distributions in nanocrystalline materials from x-ray diffraction profile analysis," Philos. Mag. A **77**, 621–640 (1998).

35 C. H. Johansson, "Die thermische Ausdehnung einiger binären Mischkristallreihen," Ann. Phys. **381**, 445–454 (1925).

36 H. P. Klug and L. E. Alexander *X-Ray Diffraction Procedures: For Polycrystalline and Amorphous Materials*, 2nd ed. (Wiley-Interscience, 1974).

37 J. Markmann, V. Yamakov, and J. Weissmüller, "Validating grain size analysis from X-ray line broadening: A virtual experiment," Scr. Mater. **59**, 15–18 (2008).

38 M. Hoffmann and R. Birringer, "Elastic and plastic behavior of submicrometer-sized polycrystalline NiAl," Acta Mater. **44**, 2729–2736 (1996).

39 E. P. Papadakis, "The measurement of ultrasonic velocity," in *Ultrasonic Measurement Methods*, Physical Acoustics, edited by R. N. Thurston and A. D. Pierce (Academic Press, 1990), Vol. 19, Chap. 2, pp. 81–106.

40 C. Truell, C. Elbaum, and B. B. Chick, *Ultrasonic Methods in Solid State Physics* (Academic Press, 1969).

41 C. Braun, J. M. Dake, C. E. Krill III, and R. Birringer, "Abnormal grain growth mediated by fractal boundary migration at the nanoscale," Sci. Rep. **8**, 1592 (2018).

42 R. Birringer, C. E. Krill, and M. Klingel, "Orientation-phase-space-averaged properties of grain boundaries," Philos. Mag. Lett. **72**, 71–77 (1995).

43 B. Oberdorfer, D. Setman, E.-M. Steyskal, A. Hohenwarter, W. Sprengel, M. Zehetbauer, R. Pippan, and R. Würschum, "Grain boundary excess volume and defect annealing of copper after high-pressure torsion," Acta Mater. **68**, 189–195 (2014).

44 W. Kreher and W. Pompe, *Internal Stresses in Heterogeneous Solids* (Akademie Verlag, 1989).

45 E. Kröner, *Statistical Continuum Mechanics* (Springer, 1974).

46 P. C. Chou and N. J. Pagano, *Elasticity: Tensor, Dyadic, and Engineering Approaches* (Dover Publications, 1992).

47 D. C. Wallace, *Thermodynamics of Crystals* (Dover, 1998).

48 C. S. Barrett and T. B. Massalski, *Structure of Metals*, 3rd ed., International Series on Materials Science and Technology Vol. 35 (Pergamon, 1980).

49 Y. Fan, T. Iwashita, and T. Egami, "Energy landscape-driven non-equilibrium evolution of inherent structure in disordered material," Nat. Commun. **8**, 15417 (2017).

50 L. Battezzati, G. Riontino, M. Baricco, A. Lucci, and F. Marino, "A DSC study of structural relaxation in metallic glasses prepared with different quenching rates," J. NonCryst. Solids **61–62**, 877–882 (1984).

51 *CRC Handbook of Chemistry and Physics*, 76th ed., edited by D. R. Lide (CRC Press, 1995).

52 S. Vyazovkin, A. K. Burnham, J. M. Criado, L. A. Pérez-Maqueda, C. Popescu, and N. Sbirrazzuoli, "ICTAC kinetics committee recommendations for performing kinetic computations on thermal analysis data," Thermochim. Acta **520**, 1–19 (2011).

53 G. Gottstein and L. S. Shvindlerman, *Grain Boundary Migration in Metals: Thermodynamics, Kinetics, Applications*, CRC Series in Materials Science and Technology (CRC Press, 2009).

54 F. Despa, D. J. Wales, and R. S. Berry, "Archetypal energy landscapes: Dynamical diagnosis," J. Chem. Phys. **122**, 024103 (2005).

55 T. J. Rupert, J. R. Trelewicz, and C. A. Schuh, "Grain boundary relaxation strengthening of nanocrystalline Ni-W alloys," J. Mater. Res. **27**, 1285–1294 (2012).

56 V. N. Novikov and A. P. Sokolov, "Poisson's ratio and the fragility of glass-forming liquids," Nature **431**, 961–963 (2004).

57 G. N. Greaves, A. L. Greer, R. S. Lakes, and T. Rouxel, "Poisson's ratio and modern materials," Nat. Mater. **10**, 823–837 (2011).

58 S. Pugh, "XCII. Relations between the elastic moduli and the plastic properties of polycrystalline pure metals," Philos. Mag. J. Sci. **45**, 823–843 (1954).

59 A. Kelly, W. R. Tyson, and A. H. Cottrell, "Ductile and brittle crystals," Philos. Mag. J. Theor. Exp. Appl. Phys. **15**, 567–586 (1967).

60 J. R. Rice and R. Thomson, "Ductile versus brittle behaviour of crystals," Philos. Mag. J. Theor. Exp. Appl. Phys. **29**, 73–97 (1974).

61 E. Kröner, "Berechnung der elastischen Konstanten des Vielkristalls aus den Konstanten des Einkristalls," Z. Phys. **151**, 504–518 (1958).

62 J. J. Lewandowski, W. H. Wang, and A. L. Greer, "Intrinsic plasticity or brittleness of metallic glasses," Philos. Mag. Lett. **85**, 77–87 (2005).

63 Y. Q. Cheng, A. J. Cao, and E. Ma, "Correlation between the elastic modulus and the intrinsic plastic behavior of metallic glasses: The roles of atomic configuration and alloy composition," Acta Mater. **57**, 3253–3267 (2009).

64 F. H. Stillinger and T. A. Weber, "Packing structures and transitions in liquids and solids," Science **225**, 983–989 (1984).